nature materials

Supplementary information

https://doi.org/10.1038/s41563-024-02090-w

Dynamic flow control through active matter programming language

In the format provided by the authors and unedited

Contents

I Coarse-grained model

I.1. Overview

Active networks of microtubules and motors exhibit diverse, and sometimes seemingly contradictory, behaviors under different conditions [1, 2]. For example, both contractile [3, 4] and extensile [5] microtubule gels have been observed. Classified by symmetry, microtubule networks can exist in isotropic [6], polar [7] or nematic [5, 8] states. The active contraction in our system is mainly driven by the number density difference of the linked motors and microtubules, where the isotropic contractile forces are the central driving force. Indeed, such forces have been found to induce the active contraction of microtubule stripes [3].

In the past two decades, various coarse-grained models for motor-microtubule systems have been derived based on thermodynamic principles, such as the active gel theory [9–11], or microscopic interactions [12–14]. However, successful comparison of models and experiments for both microtubules and the ambient fluid is still lacking. Past attempts at modeling fluid flows in motor-microtubule systems are mainly through the boundary force model [4, 6], by placing force singularities at the boundaries of the illuminated region. The singularities are assumed immobile and thus the dynamics of active microtubules is not captured with this approach. Here we construct a multiphase complex fluids model that can quantitatively predict the coupled dynamics of microtubules and solvent flows.

Our system consists of three phases, namely the crosslinked microtubules, the freely-moving microtubules and the solvent solution. Other chemical species in our model include ATP and motor proteins. Upon illumination, the unlinked homodimer motor proteins will link to form tetramer motors, which can be further classified depending on whether they are bound on microtubules or not. To avoid confusion, we term the homodimer and tetramer motors "unlinked" and "linked" motors, respectively. The chemical reactions in our system include the reversible linking of motors under light and the reversible crosslinking of microtubules with linked motors. These chemical reactions will enter our model through the transport equations in section I.2.

In terms of dynamics, our system is mainly driven by the active stresses generated in the crosslinked microtubules. The stress-strain response of the crosslinked microtubules is modeled as a viscoelastic gel. The free microtubules are treated as passive particles and the solvent solution a Stokes flow. The ATP and motor proteins are much smaller molecules and assumed to follow the solvent flow, with the exception of the linked motors bound on microtubules, which follow the crosslinked microtubules. Each of the three phases also exerts friction on the other two. The momentum equations will be given in section I.3

As discussed before, we find *a posteriori* that the isotropic active stresses dominate in our system and the polar and nematic effects can be neglected. For simplicity we will not model the polarity distribution and its dynamical impacts in this paper.

I.2. Continuity Equations

The chemical reactions are sketched in Fig. S1. The motor proteins can reversibly link and the transport equations are

$$\frac{\partial m}{\partial t} + \boldsymbol{\nabla} \cdot (m\boldsymbol{u}) = 2(p^m d_f - p^d m^2) + D_m \nabla^2 m \tag{S1}$$

where m is the unlinked motor concentration, t is time, d_f is the freely-moving linked motor concentration, $\boldsymbol{u}$ is the solvent flow velocity, D_m is the diffusivity, p^m and $p^d(x, y, t)$ are the monomerization and dimerization rates of iLID proteins, respectively. For a static rectangular light bar, $p^d(x, y, t)$ is assumed to be

$$p^d(x, y, t) = \frac{p_0^d}{\left(1 + \left(\frac{x - c_x}{r_x}\right)^8\right)\left(1 + \left(\frac{y - c_y}{r_y}\right)^8\right)}, \tag{S2}$$

which is approximately a rectangular function with its center at (c_x, c_y), side lengths $2r_x$ and $2r_y$, and maximum value p_0^d. The exponent "8" is empirically chosen. In general this exponent should be an even number and a larger exponent yields a sharper boundary of the rectangle. For a rotating light bar, one just needs to rotate the above expression in the $x - y$ plane at different times.

The transport equations for the crosslinked and freely-moving microtubules are

$$\frac{\partial c}{\partial t} + \boldsymbol{\nabla} \cdot (c\boldsymbol{v}) = p_1^{on} c_f d_f - p_1^{off} c, \tag{S3a}$$

$$\frac{\partial c_f}{\partial t} + \boldsymbol{\nabla} \cdot (c_f \boldsymbol{v}_f) = -p_1^{on} c_f d_f + p_1^{off} c + D_f \nabla^2 c_f. \tag{S3b}$$

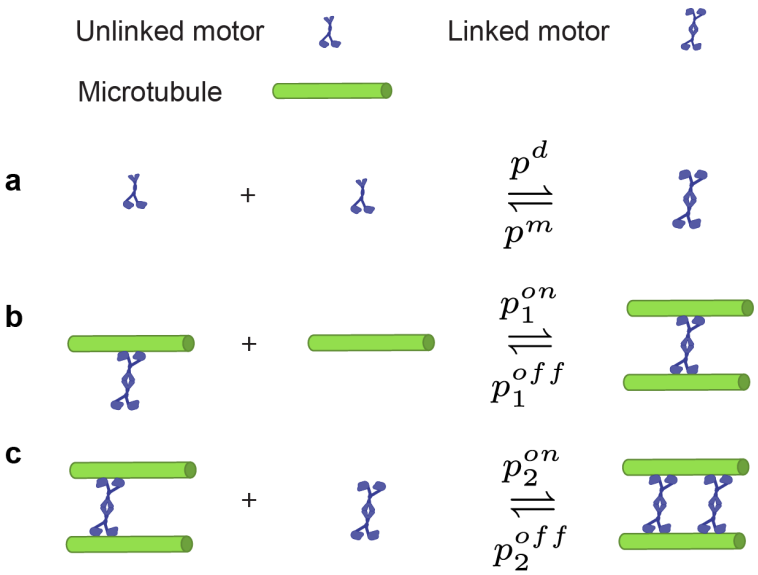

FIG. S1: **Illustrations of chemcial reactions in the model**. **a**, Reversible linking of motors. **b**, Reversible crosslinking of a freely-moving microtubule i and another microtubule j. The latter can be either free or pre-crosslinked. **c**, Reversible binding of a linked motor on two pre-crosslinked microtubules.

where D_f is the diffusivity of the freely-moving microtubules, p_1^{on} and p_1^{off} are the crosslinking and un-crosslinking rates, respectively, see Fig. S1b. The velocities of the crosslinked and freely-moving microtubules are denoted by $\boldsymbol{v}$ and $\boldsymbol{v}_f$, respectively.

The transport equations for the freely-moving and the bound linked motors are

$$\frac{\partial d_f}{\partial t} + \boldsymbol{\nabla}\cdot(d_f\boldsymbol{u}) = -p^m d_f + p^d m^2 - p_1^{on} c_f d_f - p_2^{on} c d_f + p_2^{off} d_b + D_d \nabla^2 d_f \tag{S4a}$$

$$\frac{\partial d_b}{\partial t} + \boldsymbol{\nabla}\cdot(d_b\boldsymbol{v}) = p_1^{on} c_f d_f + p_2^{on} c d_f - p_2^{off} d_b, \tag{S4b}$$

where d_b is the bound linked motor concentration, p_2^{on} is the rate of the linked motors binding on the crosslinked microtubules, D_d is the diffusivity of the free linked motors, p_2^{off} is the unbinding rate of a linked motor without uncrosslinking the two microtubules, see Fig. S1c. All freely-moving motors are assumed to follow the solvent flow and the bound motors follow the crosslinked gel.

The transport equation for the ATP is

$$\frac{\partial c_A}{\partial t} + \boldsymbol{\nabla}\cdot(c_A\boldsymbol{u}) = -k_A d_b c_A + D_A \nabla^2 c_A, \tag{S5}$$

where k_A is the consumption rate of the ATP by the bound linked motors, and D_A is the ATP diffusivity. The continuity equation for the solvent flow is

$$\boldsymbol{\nabla}\cdot\boldsymbol{u} = 0. \tag{S6}$$

I.3. Momentum Equations

We find it crucial to model the crosslinked and freely-moving microtubules as two separate phases. The former can be modeled as a self-contracting active gel and the latter passive particles. The solvent flow is assumed to be a Stokes flow. In this section, we list the momentum equations for each phase.

I.3.1. Crosslinked microtubules as an active gel

The crosslinked microtubules form an active gel, which is assumed to be viscoelastic. The momentum equation can be written as

$$\boldsymbol{\nabla}\cdot(\boldsymbol{\sigma}_a + \boldsymbol{\sigma}_v + \boldsymbol{\sigma}_{el} + \boldsymbol{\sigma}_{st}) + \boldsymbol{f}_{fl} + \boldsymbol{f}_f = \boldsymbol{0}, \tag{S7}$$

where $\boldsymbol{\sigma}_a$, $\boldsymbol{\sigma}_v$, $\boldsymbol{\sigma}_{el}$ and $\boldsymbol{\sigma}_{st}$ are the active, viscous, elastic and steric stresses in the gel, $\boldsymbol{f}_{fl}$ and $\boldsymbol{f}_f$ are the frictions with the solvent and freely-moving microtubules, respectively. Their explicit expressions can be derived from microscopic interactions [13, 14]. The active contractile stress is assumed to be

$$\boldsymbol{\sigma}_a = \alpha c_A d_b c \boldsymbol{I}, \tag{S8}$$

where c, c_A and d_b are the concentrations of the crosslinked microtubules, ATP and the bound linked motors, respectively, α is a constant activity coefficient and $\boldsymbol{I}$ is the identity tensor. This active stress is derived to be $\boldsymbol{\sigma}'_a \propto c^2 \boldsymbol{I}$, in Ref [14], where the bound motor concentration is implicitly assumed to be uniform and does not appear in active stresses. In our experiments, the concentration difference of the linked motors inside and outside of the illuminated regions is the key to form active gels. We can modify the theory in Ref [14] by adding a prefactor d_b/c in the active stresses, which is the number of bound motors per microtubule. In another word, the expression (S8) can be derived using the same methods in Ref [14] by taking the motor concentration into account and assuming the activity is proportional to the ATP concentration.

The viscous stress is

$$\boldsymbol{\sigma}_v = \eta d_b c \left(\boldsymbol{\nabla v} + \boldsymbol{\nabla v}^T\right), \tag{S9}$$

where $\boldsymbol{v}$ is the velocity of the crosslinked microtubules and η is the viscosity coefficient. This viscous stress in Ref [14] is $\boldsymbol{\sigma}'_v \propto c^2 \left(\boldsymbol{\nabla v} + \boldsymbol{\nabla v}^T\right)$. In our model the coefficient is changed from c^2 to $d_b c$ to incorporate the effects of the motor concentrations.

The elastic stress $\boldsymbol{\sigma}_{el}$ is assumed to follow the Oldroyd-Maxwell model with a long relaxation time [15],

$$\frac{\mathrm{D}\boldsymbol{\sigma}_{el}}{\mathrm{D}t} - \left[\boldsymbol{\sigma}_{el} \cdot \boldsymbol{\nabla v} + \boldsymbol{\nabla v}^T \cdot \boldsymbol{\sigma}_{el}\right] = \eta_{el} d_b c \left(\boldsymbol{\nabla v} + \boldsymbol{\nabla v}^T\right) - p_1^{off} \boldsymbol{\sigma}_{el}, \tag{S10}$$

where η_{el} is the elasticity coefficient and $\mathrm{D}/\mathrm{D}t$ is the material derivative. The steric stress is

$$\boldsymbol{\sigma}_{st} = -\xi c^2 \boldsymbol{I}, \tag{S11}$$

with a constant coefficient ξ.

The friction with freely-moving microtubules is

$$\boldsymbol{f}_f = \beta c c_f (\boldsymbol{v}_f - \boldsymbol{v}), \tag{S12}$$

where β is the friction coefficient. The friction with the solvent flow is

$$\boldsymbol{f}_{fl} = \gamma c (\boldsymbol{u} - \boldsymbol{v}) \tag{S13}$$

with the drag coefficient γ. In general the hydrodynamic drag coefficient depends on the fiber orientation [16]. In this paper we neglect the polarity in both active stresses and hydrodynamic friction.

I.3.2. Freely-moving microtubules

The freely-moving microtubules are passive particles that only experience frictions from the gel and the ambient fluid. The force balance is $\beta c_f c \left(\boldsymbol{v} - \boldsymbol{v}_f\right) + \gamma c_f (\boldsymbol{u} - \boldsymbol{v}_f) = \boldsymbol{0}$, and their velocity is therefore

$$\boldsymbol{v}_f = \frac{\beta c \boldsymbol{v} + \gamma \boldsymbol{u}}{\beta c + \gamma}. \tag{S14}$$

I.3.3. Solvent flows

The flow cells used in the experiments are typical Hele-Shaw cells, the horizontal dimensions ($x-$ and $y-$direction) of which greatly exceed their vertical dimension (z-direction). We now derive the averaged flow equation in the $xy-$plane. The three-dimensional momentum equation is

$$-\widetilde{\boldsymbol{\nabla}}\widetilde{\Pi} + \mu \widetilde{\nabla}^2 \widetilde{\boldsymbol{u}} + \gamma \widetilde{c} \left(\widetilde{\boldsymbol{v}} - \widetilde{\boldsymbol{u}}\right) + \gamma \widetilde{c}_f \left(\widetilde{\boldsymbol{v}}_f - \widetilde{\boldsymbol{u}}\right) = 0, \tag{S15}$$

where $\widetilde{\Pi}$ and μ are the fluid pressure and viscosity, respectively. We use a tilde "$\sim$" on top to indicate the variable is a function of (x, y, z) and if the variable is a vector, it is a three-dimensional vector, e.g., $\widetilde{\Pi} = \widetilde{\Pi}(x, y, z)$ and

$\widetilde{\boldsymbol{u}}(x,y,z)=(\widetilde{u}_x(x,y,z),\widetilde{u}_y(x,y,z),\widetilde{u}_z(x,y,z))$. Since the vertical length scale is much smaller than horizontal length scales, the classical lubrication theory [16] shows that $\widetilde{\Pi}(x,y,z)\approx\Pi(x,y)$, i.e., the fluid pressure is constant along z-direction, and $\widetilde{u}_z\approx 0$. Substituting these two results into equation (S15) yields $\widetilde{v}_z\approx 0$ and $\widetilde{v}_{f,z}\approx 0$. Furthermore, the $x-$ and $y-$components of equation (S15) can be approximated by

$$-\boldsymbol{\nabla}\Pi+\mu\frac{\partial^2\widetilde{\boldsymbol{u}}}{\partial z^2}+\gamma\widetilde{c}\left(\widetilde{\boldsymbol{v}}-\widetilde{\boldsymbol{u}}\right)+\gamma\widetilde{c}_f\left(\widetilde{\boldsymbol{v}}_f-\widetilde{\boldsymbol{u}}\right)=0, \tag{S16}$$

where all vectors only have $x-$ and $y-$components, i.e., $\widetilde{\boldsymbol{u}}=(\widetilde{u}_x(x,y,z),\widetilde{u}_y(x,y,z))$, $\widetilde{\boldsymbol{v}}=(\widetilde{v}_x(x,y,z),\widetilde{v}_y(x,y,z))$ and $\widetilde{\boldsymbol{v}}_f=(\widetilde{v}_{f,x}(x,y,z),\widetilde{v}_{f,y}(x,y,z))$. Therefore, the analytical solution of $\widetilde{\boldsymbol{u}}$ requires knowledge of the three-dimensional distribution of $\widetilde{c}$, $\widetilde{\boldsymbol{v}}$ and $\widetilde{\boldsymbol{v}}_f$. To derive a two-dimensional model, we further simplify equation (S16) by replacing the frictions with their z-directional average, i.e.,

$$-\boldsymbol{\nabla}\Pi+\mu\frac{\partial^2\widetilde{\boldsymbol{u}}}{\partial z^2}+\gamma c\left(\boldsymbol{v}-\boldsymbol{u}\right)+\gamma c_f\left(\boldsymbol{v}_f-\boldsymbol{u}\right)=0, \tag{S17}$$

where $c(x,y)=h^{-1}\int_0^h\widetilde{c}\mathrm{d}z$, $\boldsymbol{v}(x,y)=h^{-1}\int_0^h\widetilde{\boldsymbol{v}}\mathrm{d}z$, $\boldsymbol{v}_f(x,y)=h^{-1}\int_0^h\widetilde{\boldsymbol{v}}_f\mathrm{d}z$, and $\boldsymbol{u}(x,y)=h^{-1}\int_0^h\widetilde{\boldsymbol{u}}\mathrm{d}z$ with the top and bottom walls of channel at $z=0$ and $z=h$, respectively. These notations are consistent with the rest of the paper. The solution of equation (S17) is

$$\widetilde{\boldsymbol{u}}=\frac{1}{2\mu}\left[\boldsymbol{\nabla}\Pi-\gamma c\left(\boldsymbol{v}-\boldsymbol{u}\right)-\gamma c_f\left(\boldsymbol{v}_f-\boldsymbol{u}\right)\right]z(z-h). \tag{S18}$$

Combining $\boldsymbol{u}=h^{-1}\int_0^h\widetilde{\boldsymbol{u}}\mathrm{d}z$ and equations (S14) and (S18), we have the average two-dimensional flow velocity

$$\boldsymbol{u}=-\frac{h^2}{12\mu}\left[\boldsymbol{\nabla}\Pi-\left(\gamma c+\gamma_f c_f\right)\left(\boldsymbol{v}-\boldsymbol{u}\right)\right], \tag{S19}$$

with $\gamma_f=\gamma\beta c/(\beta c+\gamma)$. The above result is a modified Darcy's law in a Hele-Shaw cell [16] by incorporating the microtubule friction.

I.4. Non-dimensionalization

Using the initial microtubule concentration c_0, initial unlinked motor concentration m_0, initial ATP concentration c_{A0}, and the typical length scale of the illuminated region l, we can non-dimensionalize the governing equations by

$$\begin{gathered}\overline{c}=\frac{c}{c_0},\quad\overline{\boldsymbol{\nabla}}=l_0\boldsymbol{\nabla},\quad\overline{m}=\frac{m}{m_0},\quad\overline{d}_f=\frac{d_f}{m_0},\quad\overline{d}_b=\frac{d_b}{m_0},\quad\overline{c}_A=\frac{c_A}{c_{A0}}\\ \overline{t}=\frac{t}{t_0},\quad\overline{\boldsymbol{v}}=\frac{\boldsymbol{v}}{v_0},\quad\overline{\boldsymbol{v}}_f=\frac{\boldsymbol{v}_f}{v_0},\quad\overline{\boldsymbol{u}}=\frac{\boldsymbol{u}}{v_0},\quad\overline{\boldsymbol{\sigma}}_{el}=\frac{\boldsymbol{\sigma}_{el}}{\sigma_0},\quad\overline{\Pi}=\frac{\Pi}{\Pi_0},\end{gathered} \tag{S20}$$

where we use overlines to denote dimensionless variables, t_0, v_0, σ_0 and Π_0 are typical scales of time, velocity, stress, and fluid pressure, respectively. By balancing the contractile stress (S8) and the viscous stress (S9) in the active gel, we have $v_0=\alpha c_{A0}l/\eta$. The typical time scale follows as $t_0=l_0/v_0=\eta/\alpha c_{A0}$. The typical stress scale can be obtained from equation (S8), which is $\sigma_0=\alpha c_{A0}c_0m_0$. From equation (S19), we have $\Pi_0=c_0\gamma v_0l_0=\alpha\gamma c_0c_{A0}l_0^2/\eta$.

The dimensionless transport equations for the unlinked (S1) and linked (S4) motors are

$$\frac{\partial\overline{m}}{\partial\overline{t}}+\overline{\boldsymbol{\nabla}}\cdot\left(\overline{m}\overline{\boldsymbol{u}}\right)=2(\overline{p}^m\overline{d}_f-\overline{p}^d\overline{m}^2)+\mathrm{Pe}_m^{-1}\overline{\nabla}^2\overline{m}, \tag{S21a}$$

$$\frac{\partial\overline{d}_f}{\partial\overline{t}}+\overline{\boldsymbol{\nabla}}\cdot\left(\overline{d}_f\overline{\boldsymbol{u}}\right)=-\overline{p}^m\overline{d}_f+\overline{p}^d\overline{m}^2-\overline{p}_1^{on}\overline{c}_f\overline{d}_f-\overline{p}_2^{on}\overline{c}\overline{d}_f+\overline{p}_2^{off}\overline{d}_b+\mathrm{Pe}_d^{-1}\overline{\nabla}^2\overline{d}_f, \tag{S21b}$$

$$\frac{\partial\overline{d}_b}{\partial\overline{t}}+\overline{\boldsymbol{\nabla}}\cdot\left(\overline{d}_b\overline{\boldsymbol{v}}\right)=\overline{p}_1^{on}\overline{c}_f\overline{d}_f+\overline{p}_2^{on}\overline{c}\overline{d}_f-\overline{p}_2^{off}\overline{d}_b, \tag{S21c}$$

where the dimensionless reaction coefficients are $\overline{p}^m=p^mt_0$, $\overline{p}^d=p^mm_0t_0$, $\overline{p}_1^{on}=p_1^{on}c_0t_0$, $\overline{p}_2^{on}=p_2^{on}c_0t_0$ and $\overline{p}_2^{off}=p_2^{off}t_0$. We use Pe to denote the Péclet number and $\mathrm{Pe}_m=v_0l/D_m$, $\mathrm{Pe}_d=v_0l/D_d$.

The dimensionless transport equations for the microtubules (S3) are

$$\frac{\partial\overline{c}}{\partial\overline{t}}+\overline{\boldsymbol{\nabla}}\cdot\left(\overline{c}\overline{\boldsymbol{v}}\right)=\overline{p}_1^{on}\overline{c}_f\overline{d}_f-\overline{p}_1^{off}\overline{c}, \tag{S22a}$$

$$\frac{\partial\overline{c}_f}{\partial\overline{t}}+\boldsymbol{\nabla}\cdot\left(\overline{c}_f\overline{\boldsymbol{v}}_f\right)=-\overline{p}_1^{on}\overline{c}_f\overline{d}_f+\overline{p}_1^{off}\overline{c}+\mathrm{Pe}_f^{-1}\overline{\nabla}^2\overline{c}_f \tag{S22b}$$

with $\overline{p}_1^{off} = p_1^{off} t_0$, $\mathrm{Pe}_f = v_0 l_0 / D_f$. For ATP, equation (S5) becomes

$$\frac{\partial \overline{c}_A}{\partial \overline{t}} + \overline{\boldsymbol{\nabla}} \cdot (\overline{c}\overline{\boldsymbol{u}}) = -\overline{k}_A \overline{d}_b \overline{c}_A + Pe_A^{-1} \overline{\nabla}^2 \overline{c}_A, \tag{S23}$$

where $\overline{k}_A = k_A m_0 t_0$ and $\mathrm{Pe}_A = v_0 l_0 / D_A$.

The continuity equation for the solvent flow (S6) is

$$\overline{\boldsymbol{\nabla}} \cdot \overline{\boldsymbol{u}} = 0. \tag{S24}$$

Using equations (S7-S14), the dimensionless momentum equations for the active gel are

$$\overline{\boldsymbol{\nabla}} \cdot \left[\left(\overline{c}_A \overline{d}_b \overline{c} - \overline{\xi} \overline{c}^2 \right) \boldsymbol{I} + \overline{\boldsymbol{\nabla}} \overline{\boldsymbol{v}} + \overline{\boldsymbol{\nabla}} \overline{\boldsymbol{v}}^T + \overline{\boldsymbol{\sigma}}_{el} \right] + \left(\overline{\gamma}_f \overline{c}_f + \overline{\gamma c} \right) \left(\overline{\boldsymbol{u}} - \overline{\boldsymbol{v}} \right) = \boldsymbol{0} \tag{S25}$$

where $\overline{\xi} = \xi c_0 / \alpha c_{A0} m_0$, $\overline{\gamma} = \gamma l_0^2 / m_0 \eta$, $\overline{\gamma}_f = \gamma_f l_0^2 / m_0 \eta$ and

$$\frac{\mathrm{D}\overline{\boldsymbol{\sigma}}_{el}}{\mathrm{D}\overline{t}} - \left[\overline{\boldsymbol{\sigma}}_{el} \cdot \overline{\boldsymbol{\nabla}} \overline{\boldsymbol{v}} + \overline{\boldsymbol{\nabla}} \overline{\boldsymbol{v}}^T \cdot \overline{\boldsymbol{\sigma}}_{el} \right] = \overline{\eta}_{el} \overline{d}_b \overline{c} \left(\overline{\boldsymbol{\nabla}} \overline{\boldsymbol{v}} + \overline{\boldsymbol{\nabla}} \overline{\boldsymbol{v}}^T \right) - \overline{p}_1^{off} \overline{\boldsymbol{\sigma}}_{el}, \tag{S26}$$

with $\overline{\eta}_{el} = \eta_{el} / \alpha c_{A0}$.

The dimensionless velocity of the freely-moving microtubules (S14) is

$$\overline{\boldsymbol{v}}_f = \frac{\overline{\beta}\overline{c}\overline{\boldsymbol{v}} + \overline{\gamma}\overline{\boldsymbol{u}}}{\overline{\beta}\overline{c} + \overline{\gamma}}, \tag{S27}$$

with $\overline{\beta} = \beta l_0^2 c_0 / m_0 \eta$. Note that only two of $\overline{\beta}$, $\overline{\gamma}$ and $\overline{\gamma}_f$ are independent, which are connected through $\overline{\gamma}_f = \overline{\gamma}\overline{\beta}\overline{c} / (\overline{\beta}\overline{c} + \overline{\gamma})$.

The dimensionless solvent flow (S19) is

$$\overline{\boldsymbol{u}} = -\overline{\zeta} \left[\overline{\boldsymbol{\nabla}} \overline{\Pi} - \left(\overline{c} + \frac{\overline{\gamma}_f}{\overline{\gamma}} \overline{c}_f \right) \left(\overline{\boldsymbol{v}} - \overline{\boldsymbol{u}} \right) \right], \tag{S28}$$

with $\overline{\zeta} = h^2 c_0 \gamma / 12 \mu$.

I.5. Simulations

I.5.1. Physical parameters

All experiments in the paper are controlled to be at similar conditions. Therefore, the same physical parameters are used in simulations throughout the paper, with one exception in Fig. 2c in the main text where $\overline{\zeta}$ is varied. The physical parameters are documented below:

$$\begin{gathered} l_0 = 240\ \mu\mathrm{m}, \quad t_0 = 40\ \mathrm{s}, \quad p_0^d = 15, \quad p^m = 12, \quad p_1^{on} = 15, \quad p_2^{on} = 0.75, \\ p_1^{off} = 10, \quad p_2^{off} = 20, \quad \mathrm{Pe}_f^{-1} = 10^{-3}, \quad \mathrm{Pe}_m^{-1} = \mathrm{Pe}_d^{-1} = \mathrm{Pe}_A^{-1} = 10^{-2}, \\ \overline{k}_A = 0.8, \quad \overline{\xi} = 0.05, \quad \overline{\eta}_{el} = 1.5, \quad \overline{\gamma} = 0.045, \quad \overline{\beta} = 0.45, \quad \overline{\zeta} = 20.5. \end{gathered} \tag{S29}$$

Additionally, the duration of each light pulse is 0.04 and the time interval between two light pulses is 0.2.

I.5.2. Aspect ratios of single bars

In the main text we show that the bar sizes do not affect the power law of flow decay. Another important geometric factor is the aspect ratio. A previous study on flows generated with different aspect ratios (AR) [6] shows that they can change the flow directions outside the light bar: when AR ≥ 0.5, the flow is directed away from the light region, as opposed to when AR ≤ 0.25, the flow goes into the light bar.

To understand how the AR of a rectangular light bar affects scaling of flow decay, we fix the bar width and simulate single-bar flows with different aspect ratios. The center-line flow magnitudes are documented in Fig. S2. Fig. S2a shows that aspect ratios can change flow directions. When AR≤ 0.25, the center-line flow is always pointing towards the bar center. When AR≥ 0.5, the flow near the light bar edge is an outflow, pointing away from the bar. These findings are consistent with experiments [6]. Furthermore, our numerical results reveal that the flows outside the illuminated regions always decay in a power law, with the exponents ranging from -4 to -3.5, regardless of the aspect ratios (Fig. S2b). To provide experimental evidence, we measure the center-line flow field induced by a single light bar with AR$= 0.3$ in Fig. S2c. Both experimental and simulated data show that the flow decay follows the power law $(x/w)^{-3.5}$ outside the illumination region.

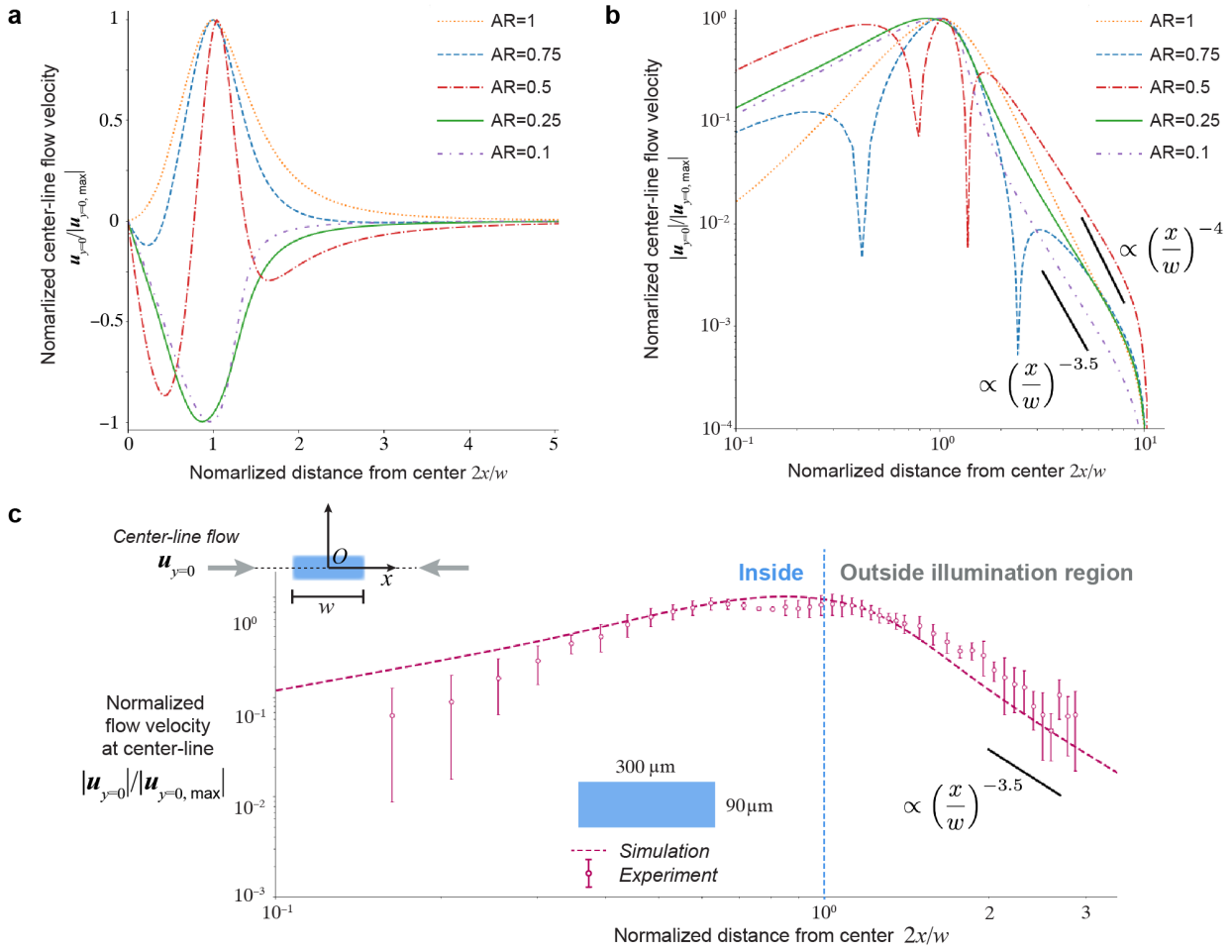

FIG. S2: **a**, Simulated center-line flows induced by single bars with different aspect ratios (AR). Positive (negative) values represent the flow is directed away from (into) the light bar. **b**, Absolute values of data in **a** in a log-log plot. **c**, Measured and simulated center-line flow field induced by a single bar with AR= 0.3. The flow fields are time-averaged over 240 s. Data are presented by mean values ± SD of 5 experiments.

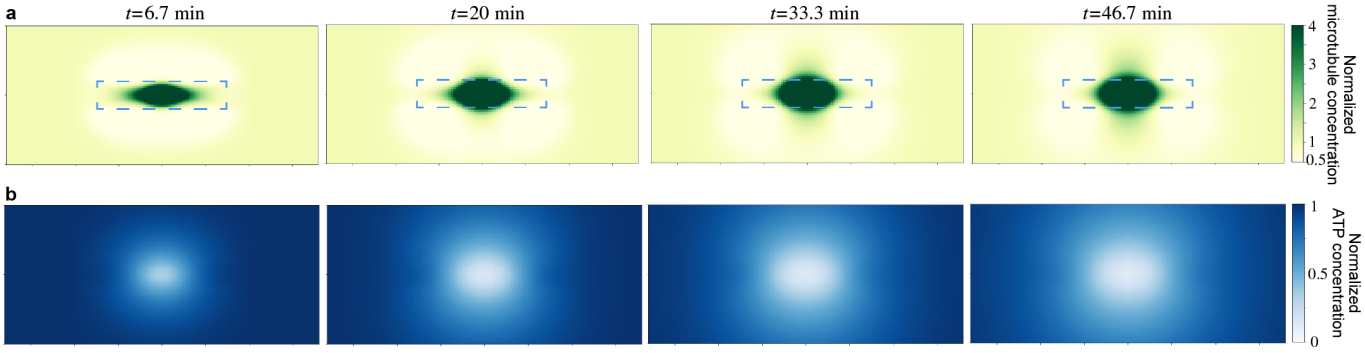

FIG. S3: **a**, Microtubule and **b**, ATP concentration field under a single light bar in simulations. The dashed line in **a** shows the light bar boundary. Both microtubule and ATP concentrations are normalized by their initial conditions.

I.5.3. ATP consumption

ATP is the power source of our system and we calculate the time course of ATP in simulations in Fig. S3. As the microtubule-kinesin aster forms a dense core, the consumption of ATP increases and results in a local depletion that cannot be sufficiently replenished by transport of ATP. More work will be done in future to characterize how ATP affects the flow intensity and stability.

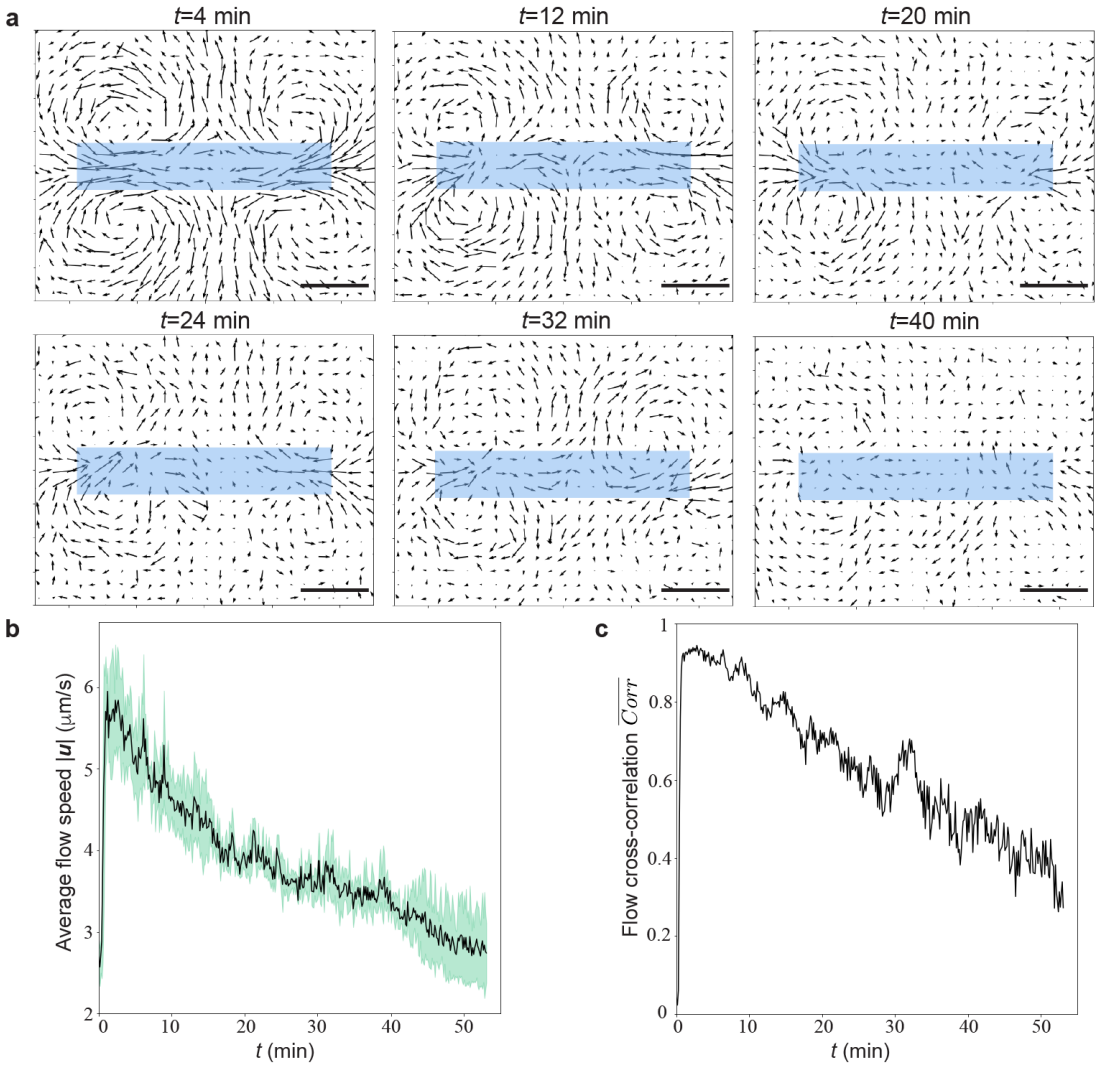

FIG. S4: Experimental flow characterization. **a**, Measured flow field over time. The flow fields are averaged over 5 experiments. Scale bars, 100 μm. **b**, Average flow magnitude over time. The flow speed is spatially averaged in the 500×400 μm rectangular region in **a**. Data are presented as mean values ± SD of 5 experiments. **c**, Cross-correlation of the flow field over time. The flow field is averaged over 5 experiments.

II Experimental system characterization

II.1. Stability of the solvent flow structure

How long does it take for our system to build up a structured solvent flow and how long can the flow persist? To address these questions, we measure the average flow speed around the light bar over time in Fig. S4a. The time course of the average flow speed in the rectangular region in Fig. S4a is plotted in Fig. S4b. We find that the flow can be quickly initiated and reach its maximum value, around 6 μm/s, within 3 min. Then the active flow slowly decays over a time span of approximately 60 min. To quantify how stable the flow structure persists, we calculate the cross-correlation of the flow field over time in Fig. S4c. The pointwise cross-correlation $Corr(x, y, t)$ is defined by $Corr(x, y, t) = \frac{\boldsymbol{u}(x,y,t)\cdot\boldsymbol{u}_0(x,y)}{|\boldsymbol{u}(x,y,t)||\boldsymbol{u}_0(x,y)|}$, where we first compute the inner product of the experimental flow field $\boldsymbol{u}(x, y, t)$ and a benchmark flow field $\boldsymbol{u}_0(x, y)$, and then normalize by their norms. The benchmark flow field $\boldsymbol{u}_0(x, y)$ is chosen to be the time average of the flow field between $t = 1$ and 10 min. We calculate the spatial average of the cross-correlation $Corr(x, y, t)$ in the 500 × 400 μm region shown in Fig. S4a, which is denoted by $\overline{Corr}(t)$ and plotted in Fig. S4a. The range of $\overline{Corr}(t)$ is $[-1, 1]$ where $\overline{Corr}(t) = 1$ represents perfect alignment of the experimental flow field with the benchmark flow. Both the average flow magnitude and cross-correlation decay monotonously after t =3 min. The flow magnitude drops to its medium value 4 μm/s at around t =20 min, when the cross-correlation $\overline{Corr}(t = 20$ min) is 0.7. Additionally, Fig. S4a shows that the flow field at t =20 min can clearly maintain its four-vortex structure. These

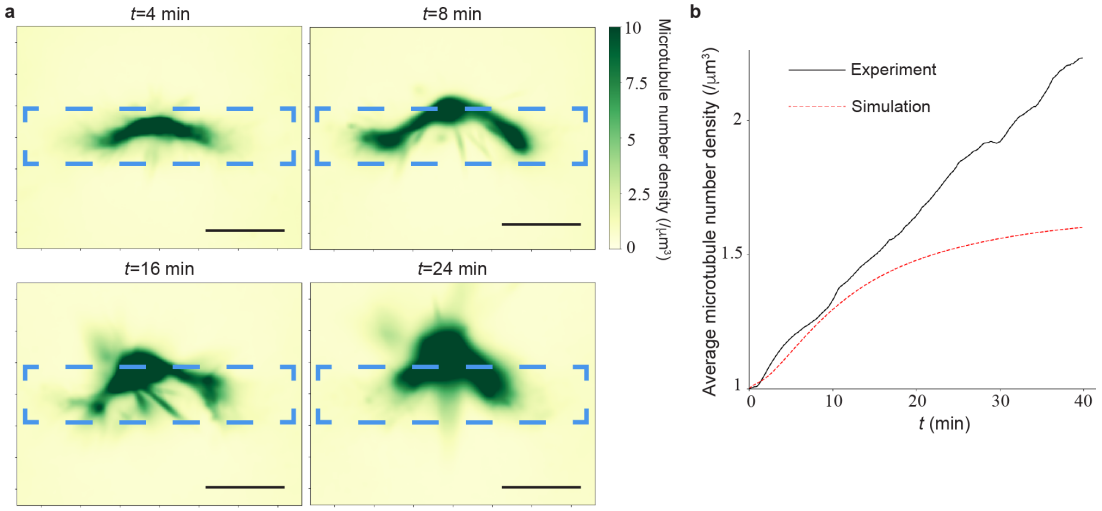

FIG. S5: Microtubule concentration characterization. **a**, Microtubule concentration field generated by a single light bar. The boundary of the light bar is labeled by a dashed line. Scale bars, 50 μm. **b**, Average microtubule concentration over time. The microtubule concentration is spatially averaged in the 180×140 μm rectangular region in **a**.

results suggest that our active solvent flow can maintain its intensity and structure over a time span of 20 min, which is also the time scale for applications.

II.2. Microtubule concentration field

We also measure the time course of microtubule concentration generated by a single bar in Fig. S5 The microtubule concentration is measured by the fluorescent intensity of Cy5 tagged on microtubules, where a linear relationship has been confirmed in our other paper [17]. Fig. S5a shows the spatial distribution of microtubules over time and Fig. S5b shows the average microtubule concentration in the rectangular region in Fig. S5a. The question of concern is how the accumulation of microtubules affects the flow field. The active solvent flow is driven by the microtubule fluxes going into the two short sides of the light bar. On the one hand the accumulation of microtubules could generate a higher active stress that might strengthen the flow, on the other hand the dense microtubule aster could increase flow resistance inside the channel and thus might decrease the flow. Fig. S5b shows that average microtubule concentration in the aster grows linearly with time in experiments. As a consequence, the average mass flux of microtubules going into the aster is constant in time, which indicates that the accumulation of kinesin motors inside the microtubule network is not able to recruit more active matter influxes over time. As the flow resistance in the channel increases with the microtubule concentration, the flow strength decreases in time, as shown in Fig. S4b. Fig. S4b and Fig. S5b demonstrate that the active matter system is more efficient in driving solvent flows when the aster is not dense. The exact mechanisms of the optimal microtubule network density and its values under different physical and chemical conditions remain an open question.

The time course of average microtubule concentration in simulations is also shown in Fig. S5b. Up to t=15 min, the simulated microtubule concentration also increases linearly. However, it plateaus at later times. The discrepancy between simulations and experiments may be due to neglecting higher-order active stresses in our model. Our model only considers the isotropic active stresses while the polar and nematic effects are neglected. At late times, such higher-order effects can be important when the microtubule aster is dense, which can result in dynamic and unstable shapes as shown in Fig. S5a. These unstable shapes are not reproducible with our current model. Furthermore, our model assumes a simple isotropic steric stress that is quadratic in the microtubule concentration, which could be too strong such that the microtubule concentration plateaus at late times. Future efforts will be including these high-order effects in both active and steric stresses.

II.3. Microtubule length distribution

The microtubule length calculation begins with image normalization to account for background intensities across samples. We then apply a combination of local and global thresholding techniques to segment microtubules from the

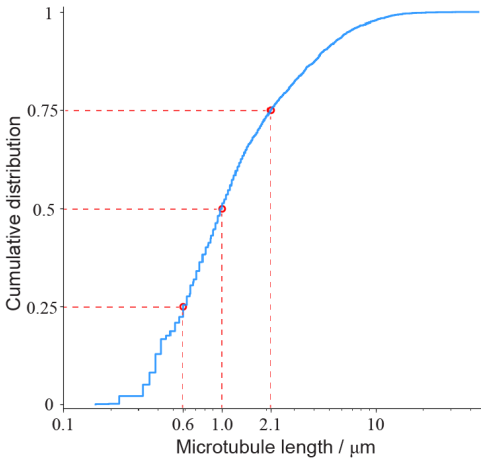

FIG. S6: Cumulative distribution of microtubule lengths.

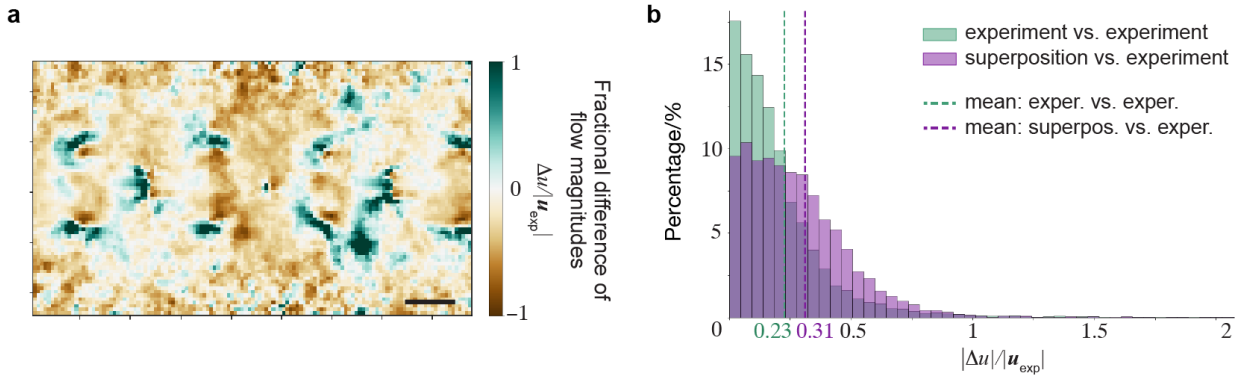

FIG. S7: **a**, Comparison of flow magnitudes between two-bar experiments and superposition of 2 single-bar flows. The heatmap represents the fractional difference between measured and superposed flow magnitudes $\Delta u/|\boldsymbol{u}_{\rm exp}|$, where $\Delta u = |\boldsymbol{u}_{\rm sup}| - |\boldsymbol{u}_{\rm exp}|$. **b**, Distributions of discrepancy in **a** and experimental variations. This demonstrates that the superposition-induced discrepancy is relatively small, only increasing the mean of errors from 0.23 to 0.31. All scale bars are 100 μm and all flow fields are time-averaged from $t = 160$ s to 400 s.

background, adapting to local intensity variations while maintaining consistent overall detection sensitivity. Morphological operations are used to refine the segmented structures, closing small gaps in filaments that may result from thresholding. To improve measurement accuracy, we implement several artifact removal steps: objects touching image borders are excluded to avoid partial measurements, small objects below a size threshold are removed to reduce noise, and circular objects are filtered out based on eccentricity to focus on linear microtubule structures. The data and codes been deposited at https://github.com/fy26/ActiveMatter/tree/main/Microtubule%20length%20distribution. The measured cumulative distribution function of microtubule lengths is plotted in Fig. S6. The median length is 1.0 μm.

II.4. Comparison of flow magnitudes between superposition and experiments

To quantify the errors introduced by superposition, we compare the flow magnitudes between the superposed flow of 2 single-bar flows and experimental measurement of 2-bar flows (Fig. S7a). The flow data are the same with Figs. 1b and 1c in the main text. We also calculate the experimental variations of flow magnitudes and compare their distribution with the superposition-induced error distribution, which is plotted in Fig. S7b. The results show that the errors induced by linear superposition are small, only increasing the mean of errors from 0.23 to 0.31.

II.5. Superposition of two pentagons

To further demonstrate that the principle of linear superposition is not limited to rectangular shapes, we experimentally show that superposition of two single-pentagon flows also matches with the flow field generated by two pentagons

in Fig. S8. The flow field induced by a single pentagonal light pattern has 10 counter-rotating vortices, as shown in Fig. S8a. Such flow structures also persist when there are two pentagonal light patterns next to each other, as shown in Fig. S8b. We linearly superpose two single-pentagon flows in Fig. S8a to match the flow in Fig. S8b. The superposed flow field and flow-direction discrepancy $\Delta\theta$ are shown in Fig. S8c. We then quantify the distribution of $\Delta\theta$ in Fig. S8d. The mean of $\Delta\theta$ is 0.58, comparable to the mean values of discrepancy found in two-bar and nine-bar superposition, which are 0.3 and 0.6, respectively. Therefore, the principle of linear superposition is not limited to rectangular bars and can be generalized to other shapes.

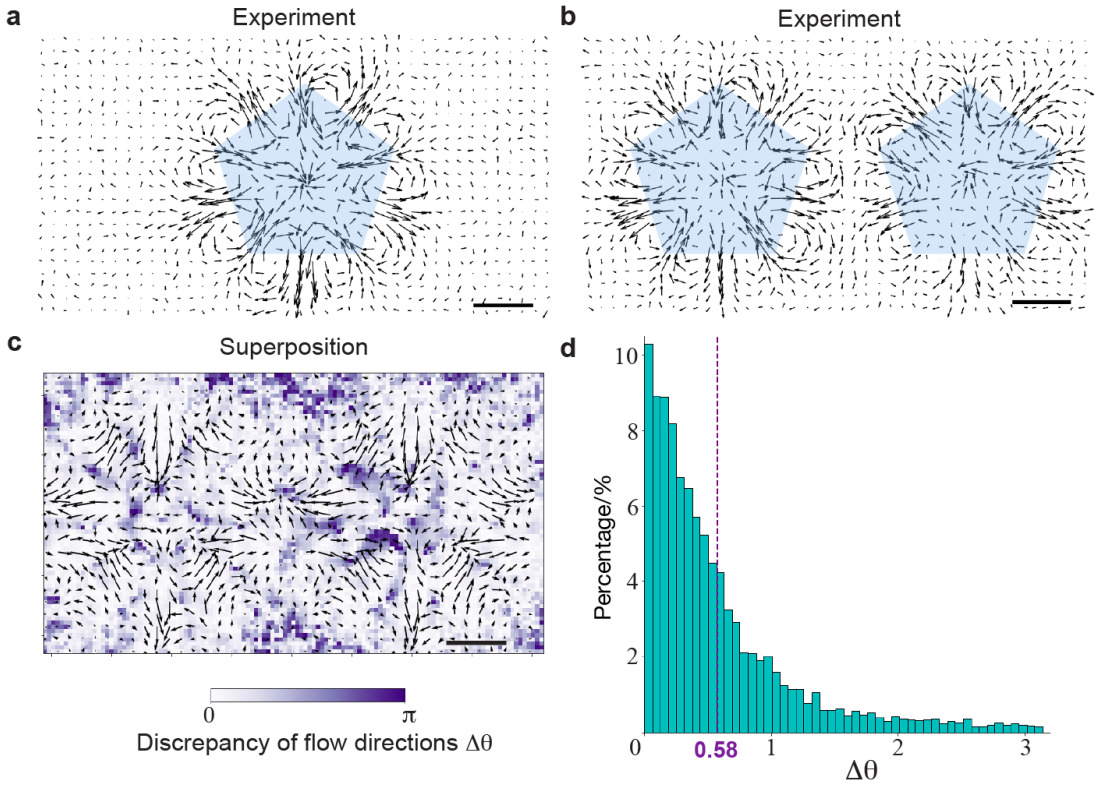

FIG. S8: Linear superposition can be applied to pentagons. **a**, Experimental flow field generated by a single pentagonal light pattern. **b**, Experimental flow field generated by two pentagons. **c**, The vector field is a superposition of two single-pentagon flows in **a** to match the flow field in **b**. The heat map shows the discrepancy of flow directions $\Delta\theta$ between superposed and measured flows. **d**, Distribution of the flow discrepancy $\Delta\theta$. The mean is 0.58. All flow fields are time-averaged over 240 s. Scale bars, 100 μm.

III Optimization scheme for particle transport

In this section we show how to optimize particle transport along a straight path using linear transformation of single-bar flow data (Fig. S9a). To ensure that the particle move along a straight path, the line segment AB should coincide with the axis of symmetry in the composition of light patterns (Fig. 3b, main text): when using only one bar, the particle should be placed at the center line perpendicular to the longer sides of the light bar to avoid being absorbed into the aster; when using two bars, the particle should move along their axis of symmetry, with a constraint that the two bars are separate above a critical spacing $\overline{w}_c$ to avoid merging; when using three bars, the optimal solution is just a sum of the solutions using one and two bars. Therefore we only need to solve for the optimal solution using two bars. This can be further simplified into finding the optimal location and orientation of a single bar to maximize f, and the second bar is just its reflection with respect to line AB. In this case, the objective function f only depends on three variables, the $\overline{x}-$ and $\overline{y}-$coordinates of the bar center, and its orientation angle. The optimal solution can be found by directly searching the maximum value over the three-dimensional optimization landscape using simulated single-bar flow data. The region $\overline{x} < \overline{w}_c + \overline{w}_y/2$, where $\overline{w}_y$ is the width of the shorter side, is prohibited due to the constraint $\overline{w}_g < \overline{w}_c$ (Fig. 3c, main text).

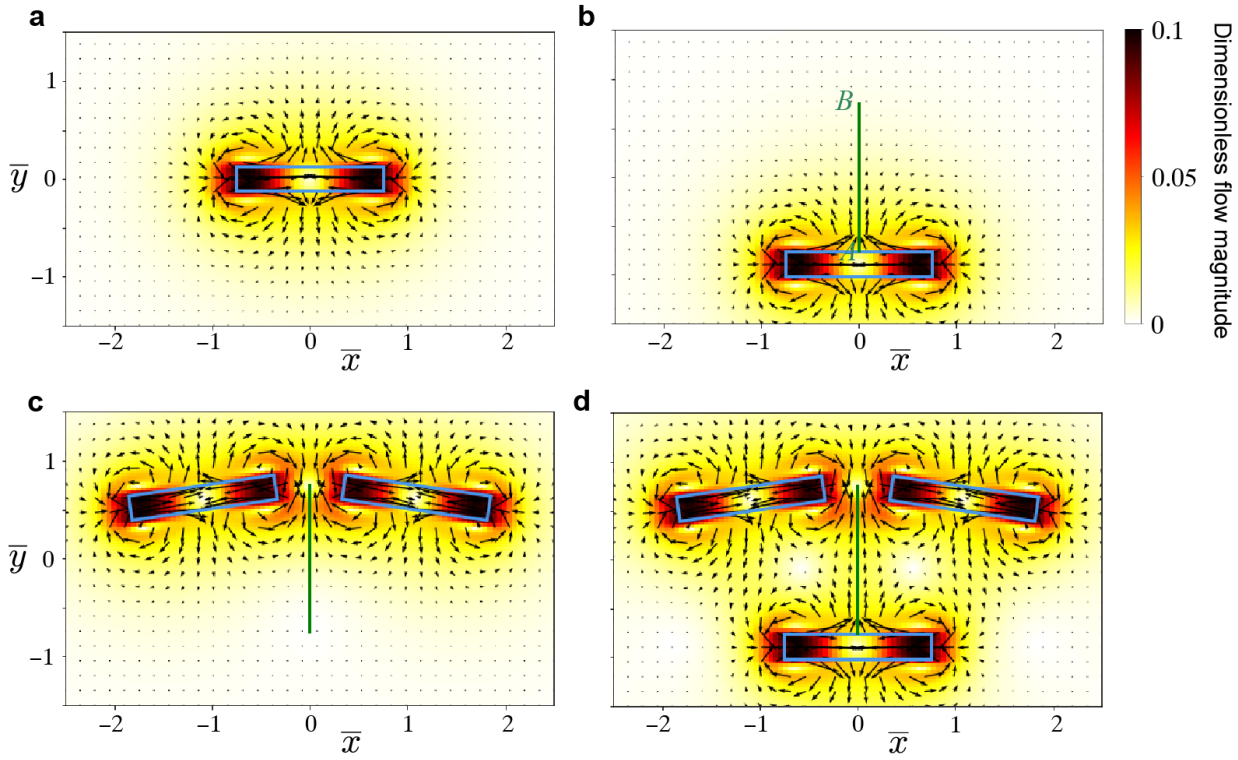

FIG. S9: **a**, Simulated single-bar flow field. Optimal solutions for particle transport using **b**, $n = 1$, **c**, $n = 2$ and **d**, $n = 3$ light bars, and their corresponding flow fields. The objective is to move a particle along the line segment AB (green). The outlines of light bars are plotted in blue.

III.1. Problem formulation

Objective: Move a particle along a line segment AB from $\overline{y} = -0.75$ to 0.75 along the $\overline{y}-$axis and maximize its speed using n bars.

The objective function is defined as

$$f = \int_A^B \overline{\boldsymbol{u}} \cdot \mathrm{d}\overline{\boldsymbol{x}}. \tag{S30}$$

The constraints are:

1. The particle does not move into the aster.

2. The spacing between bars should be above a critical length $\overline{w}_c$ to avoid interactions.

III.2. Solutions up to $n = 3$

To move the particle along a straight path, the axis of symmetry in the composition of light patterns should coincide with the $\overline{y}-$axis.

III.2.1. $n = 1$

There are two symmetry axes for a single rectangular bar (Fig. 1a, main text), and the fluid flow goes into the bar lengthwise and out of the bar breadthwise. To satisfy constraint 1, the light bar should be placed at one end of AB with its long side perpendicular to the $\overline{y}-$axis (Fig. S9b)

III.2.2. $n = 2$

When there are two bars, the only way to construct a straight streamline, except for directly using the symmetry axes of single bars, is to make the two bars symmetric about $\overline{y}$-axis. Therefore, the problem is reduced to finding the location and orientation of a single bar to maximize f, and the second bar is just its reflection with respect to $\overline{y}$-axis.

We denote the single-bar flow field in Fig. S9a as $\overline{\boldsymbol{u}}_s$. We now calculate the flow field $\overline{\boldsymbol{u}}$ induced by a single bar placed at $\overline{\boldsymbol{x}}_s$ with an orientation angle $\psi \in [0, \pi)$. The rotation matrix $\boldsymbol{R}$ associated with ψ is

$$R(\psi) = \begin{pmatrix} \cos\psi & -\sin\psi \\ \sin\psi & \cos\psi \end{pmatrix}. \tag{S31}$$

Through simple linear transformation of coordinates, the flow field $\overline{\boldsymbol{u}}$ is just

$$\overline{\boldsymbol{u}}(\overline{\boldsymbol{x}}) = R(\psi) \cdot \overline{\boldsymbol{u}}_s \left(R(\psi)^T \cdot (\overline{\boldsymbol{x}} - \overline{\boldsymbol{x}}_s) \right). \tag{S32}$$

The constraint 2 can be formulated as

$$\overline{x} - \frac{\overline{w}}{2} |\cos\psi| - \frac{\overline{w}_y}{2} \sin\psi > \frac{\overline{w}_c}{2}, \tag{S33}$$

where $\overline{w}$ and $\overline{w}_y$ are the length and breadth of the light bar.

The optimal solution can be found directly by searching for the maximum value of the objective function (S30) using (S32) and the constraint (S33), since it only depends on 3 variables. Note that in plotting the optimization landscape Fig. 3c in the main text, at each location $(\overline{x}, \overline{y})$, we first calculate the maximum value of f with respect to the orientation angle ψ and also save the optimal $\psi^*(\overline{x}, \overline{y})$. In this way, the optimal solution $(\overline{x}^*, \overline{y}^*, \psi^*(\overline{x}^*, \overline{y}^*))$ can be determined by the maximum value of f in the optimization landscape. To show how the orientation angle ψ affects the objective function f, we plot the value of f over ψ at the optimized location $(\overline{x}^*, \overline{y}^*)$ in Fig. S10.

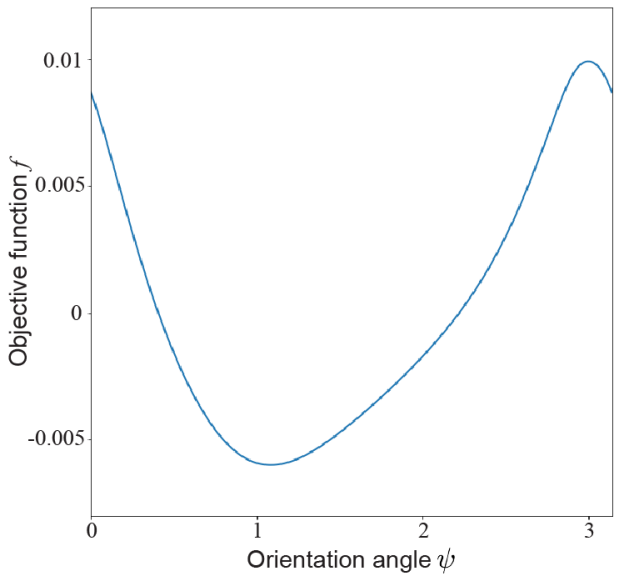

FIG. S10: Objective function f over orientation angle ψ.

Due to symmetry, there is one optimal solution in each quadrant. We can further confine the computation domain to be in Quadrant I and the solution is $\overline{x}^* = 1.09$, $\overline{y}^* = 0.62$ and $\psi^* = 3.0$ with $\overline{w}_c = 0.325$. The overall optimal two-bar configuration is shown in Fig. S9c.

III.2.3. $n = 3$

Due to symmetry, the optimal solution for 3 bars can only be the linear superposition of the optimal solutions for $n = 1$ and $n = 2$, as shown in Fig. S9d.

---

[1] M.C. Marchetti, J. F. Joanny, S. Ramaswamy, T. B. Liverpool, J. Prost, M. Rao, and R. A. Simha. Hydrodynamics of soft active matter. *Rev. Mod. Phys.*, 85:1143–1189, 2013.

[2] D. Needleman and Z. Dogic. Active matter at the interface between materials science and cell biology. *Nat. Rev. Mater.*, 2:17048, 2017.

[3] P. J. Foster, S. Fürthauer, M. J. Shelley, and D. J. Needleman. Active contraction of microtubule networks. *eLife*, 4:e10837, 2015.

[4] T. D. Ross, H. J. Lee, Z. Qu, R. A. Banks, R. Phillips, and M. Thomson. Controlling organization and forces in active matter through optically defined boundaries. *Nature*, 572:224–229, 2019.

[5] Tim Sanchez, D. T. N. Chen, S. J. DeCamp, M. Heymann, and Z. Dogic. Spontaneous motion in hierarchically assembled active matter. *Nature*, 491:431–434, 2012.

[6] Z. Qu, D. Schildknecht, S. Shadkhoo, E. Amaya, J. Jiang, H. J. Lee, D. Larios, F. Yang, R. Phillips, and M. Thomson. Persistent fluid flows defined by active matter boundaries. *Commun. Phys.*, 4:198, 2021.

[7] B. A. Dalton, D. Oriola, F. Decker, F. Jülicher, and J. Brugués. A gelation transition enables the self- organization of bipolar metaphase spindles. *Nat. Phys.*, 18:323–331, 2022.

[8] S. J. DeCamp, G. S. Redner, A. Baskaran, M. F. Hagan, and Z. Dogic. Orientational order of motile defects in active nematics. *Nat. Mater.*, 14:1110–1115, 2015.

[9] J. F. Joanny, F. Jülicher, K. Kruse, and J. Prost. Hydrodynamic theory for multi-component active polar gels. *New J. Phys.*, 9:422, 2007.

[10] J. Prost, J. F. Joanny, and F. Jülicher. Active gel physics. *Nat. Phys.*, 11:111–117, 2015.

[11] F. Jülicher, S. W Grill, and G. Salbreux. Hydrodynamic theory of active matter. *Rep. Prog. Phys.*, 81:076601, 2018.

[12] Aphrodite Ahmadi, M. C. Marchetti, and T. B. Liverpool. Hydrodynamics of isotropic and liquid crystalline active polymer solutions. *Phys. Rev. E*, 74:061913, 2006.

[13] S. Fürthauer, B. Lemma, P. J. Foster, S. C. Ems-McClung, C. H. Yu, C. E. Walczak, Z. Dogic, D. J. Needleman, and M. J. Shelley. Self-straining of actively crosslinked microtubule networks. *Nat. Phys.*, 15:1295–1300, 2019.

[14] S. Fürthauer, D. J. Needleman, and M. J. Shelley. A design framework for actively crosslinked filament networks. *New J. Phys.*, 2020.

[15] M.A. Alves, P.J. Oliveira, and F.T. Pinho. Numerical methods for viscoelastic fluid flows. *Annu. Rev. Fluid Mech.*, 53:509–541, 2021.

[16] L. G. Leal. *Advanced Transport Phenomena*. Cambridge University Press, 2007.

[17] S. Liu, R. W. Pan, H. Jin Lee, S. Shadkhoo, F. Yang, C. Li, Z. Qu, R. Phillips, and M. Thomson. Force propagation in active cytoskeletal networks, 2024.